Title

Synergy between curdlan and nanofibers of cellulose and chitin and its impact on the mechanical strength of oil-rich composite structures

Author names and affiliations

Pui Yeu Phoon,[a]* Zhan Lun Alan Tan [a]

[a] Singapore Institute of Food and Biotechnology Technology (SIFBI), Agency for Science, Technology and Research (A*STAR), 31 Biopolis Way, Singapore 138669.

Email addresses: phoon_pui_yeu@sifbi.a-star.edu.sg; alan_tan@sics.a-star.edu.sg

*Corresponding author.

Highlights

- LAOS revealed curdlan (CG)-cellulose/ chitin nanofiber (NF) synergy in paste form
- Chitin enhanced CG elasticity; cellulose increased strain stiffening in CG
- CG-NF-based oil-rich composites could yield high shear elastic modulus of ≥20 kPa
- High-compressive strain elasticity increased when CG-NF was in 1-mm stranded mesh
- With less viscous CG-cellulose phase, compression strength in composite amplified

Abstract

With alternative meats trending, research on edible oil structuring for mimicking animal fat texture is gaining traction. However, many reported cases lack universal appeal, for they are structured by proteins and/ or oleo-gelators based on steroidal or saturated fat, which may carry allergenic or cardiometabolic risks. Here, we report our discovery of synergy between curdlan (CG) and chitin (Chtn)/ cellulose (Shcel) nanofibers (NF) from small-to-large amplitude oscillatory shear experiments, and its applicative potential in fibre-based oil-rich composites as strong animal fat replacers. Some key findings are: (i) At optimised mass ratios, heat-set CG-Chtn (5:5) showed highly elastic character, while heat-set CG-ShCel (7:3) exhibited a more viscous but strain stiffening behaviour. (ii) CG-NF synergy led to derivative composites with high shear elastic modulus (G'_1) of ≥20 kPa (at ≤1% strain), similar in the order of magnitude for springy cooked pork subcutaneous fat. (iii) To improve the compressive strength in the composites, the CG-NF binary phase could form an irregular mesh framework of extruded 1 mm-strands. (iv) By manoeuvring the viscosity and pliancy of the CG-ShCel binary phase, the compressive strength could be enhanced further. Put together, these findings offer reference value for formulating strong animal fat mimetics, toward more sustainable eating.

Keywords

Emulsion gel; animal fat mimetic; food fibres; food microstructure; LAOS rheology

1. Introduction

In meat alternatives, which are hailed as food protein sources for a sustainable future, the use of unsaturated fat for a dense, fatty texture reminiscent of animal fat is limited by its textural attributes and processability. Lately, the use of food polymers to assemble a high mass fraction of oil in a heterogeneous system has been promising, in constructing structured oil with mechanical strength. This is evident from increasing reports of strengthening emulsion gels and bigels through plant proteins and/ or oleo-gelation, the latter of which is commonly achieved with copious amounts of steroidal/ saturated fat nuclei. Through these ways, shear elastic modulus (G', in Pa) could reach at least four orders of magnitude in the linear viscoelastic regime (Chen et al., 2023; Choi et al., 2024; Dreher et al., 2020; Ren et al., 2024). However, these solutions lack universal appeal due to unique allergic and cardiometabolic risks which they may bear. On the other hand, alternative approaches that steered away from the use of proteins and oleo-gelators had been published, but they tended to yield weaker emulsion gels of lower G' (Jia et al., 2022; Li et al., 2021; Zhao et al., 2024).

To fill this gap, we have been studying how to structure unsaturated edible oil into concentrated emulsion gel hybrids that are solid-like, using only natural food fibres. Particularly, we work with high shear-activated citrus fibre for its emulsifying property, and curdlan for its strong and elastic gel network induced by heating (Tan & Phoon, 2023; Tan et al., 2025). Curdlan is inherently water-insoluble and during its irreversible heat-induced gelation, single helices transform into triple helixes which align into bundles (Zhang et al., 2002). In our recent investigation, we demonstrated how laccase-oxidised ferulic acid triggered crosslinking in interfacial fibre and the strengthening of curdlan inter-triplex network, resulting in emulsion gel hybrids with increased G' under small amplitude oscillatory shear (Tan et al., 2025). However, the

order of magnitude for the attained G' (in Pa) remained at 3. In comparison, for few commercially available fatty animal parts which we priorly measured, such as cooked salmon skin, steamed chicken leg skin, and roasted pork belly fat, their G' values were in four orders of magnitude.

Seeking to increase G' in the emulsion gel hybrids further, in this work we studied the effect of adding nanofibres to the curdlan fibre network, on top of the continual use of oxidised ferulic acid. The incorporation of nanofibres to change the physical functionality of hydrocolloidal systems might not be a new concept, especially outside the field of food science. For instance, cellulose nanofibres had been proven to enhance the strength of polyvinyl alcohol and gelatin gels (Lei et al., 2019; Xu et al., 2023). Xu et al. (2023) had called attention to the exceptionally high aspect ratio of intertwining nanofibres, which could facilitate the diffusion of local stresses in hydrocolloid gels (Zhang et al., 2024) to below the trigger level for breaking network nodes. However, for ordered assemblies such as the helices of linear amylose polymers in food starch, which align into crystalline packings during starch retrogradation, the addition of bacterial cellulose nanofibres had reportedly retarded the process by interfering with amylose-amylose interaction (Zhu et al., 2017). It is not obvious whether the disruption of supramolecular orderliness by nanofibres, which caused structural weakening to amylose, would do the same to a heat-set curdlan network. There was a report on the strengthening of curdlan gel by bacterial cellulose, but at a very small cellulose-curdlan mass ratio of 2:98 (Zhou et al., 2022).

This paper explores the synergistic effect between curdlan and nanofibres of cellulose and chitin on gel strength, against a background of knowledge scarcity on curdlan displaying synergy with other hydrocolloids. To our knowledge, other reported examples of synergy were curdlan-kappa carrageenan at 1:3 mass ratio (Tao et al.,

2022) and curdlan-low acyl gellan gum for instance at 1:1 mass ratio (Zhou et al., 2024). Our interest in cellulose and chitin stems from the abundance and renewability of their source origins (Bai et al., 2022; Trache et al., 2020). Another highlight of this work is the running of strain-controlled large amplitude oscillatory shear (LAOS) experiments on curdlan-based complex systems, their composites with 50% (w/w) oil load, and cooked pork subcutaneous fat which was targeted for mimicking. Pork subcutaneous fat was chosen due to it being ubiquitous and well-loved in global cuisine for its springy texture. Under LAOS beyond the linear viscoelastic range, the stress waveforms of these materials become non-sinusoidal due to higher harmonic contributions. By analysing the higher harmonics, we present different aspects of the nonlinear viscoelasticity through Lissajous curves and the graphs of other strain-dependent parameters, e.g., relative intensity of the third harmonic in total stress I_3/I_1; elastic strain stiffening ratio; and viscous shear thinning ratio. Together, the identified subtleties in nonlinear viscoelasticity allow a more rounded physical interpretation of the complex rheological behaviour, beyond the fundamental viscoelastic moduli G'_1 and G''_1. On top of LAOS, this work also reports how curdlan-nanofibre interaction influences the compressive strength of the oil-rich composites when measured against pork subcutaneous fat. The combined insights on high strain deformation under shear and compression—two relevant key elements of stress state in normal mastication (Skamniotis et al., 2017)—will facilitate the refinement of strategies in micro-structuring curdlan-based oil-rich composites down the line, toward closer textural resemblance to the animal fat reference.

2. Materials and methods

2.1 Materials

The commercial food fibres used were as follows, with the average viscosity (η) of their native aqueous suspensions measured by cone-plate rotational rheology at 1 s^{-1} and 25°C (Supplementary material) stated alongside: chitin (Chtn) nanofibre (NF) supplied as slurry (for 2.0% w/w, η = 27 Pa.s) from Sugino Machine Ltd. (Nara City, Japan); short cellulose (ShCel) NF supplied as slurry (for 2.0% w/w, η = 10 Pa.s) from Sugino; curdlan gum (CG) powder (for 10% w/w, η = 13 Pa.s) from Natural Colloids Industries Pte. Ltd. (Singapore); and NUTRAVA® boost citrus fibre powder (for 2.0% w/w, η = 960 mPa.s) from CPKelco (Atlanta, Georgia). Ferulic acid was purchased from Penta International Corporation (West Caldwell, New Jersey). Laccase powder with 10000 U/g activity (from Aspergillus oryzae) was obtained from Sunson Industry Group Co. Ltd. (Yinchuan, China). Sunflower oil and Australian pork lard with skin were bought from a local supermarket. The common dyes Nile Red and fluorescein isothiocyanate (FITC), used for staining fat and collagen, respectively, were from leading chemical producers. Additional specific fluorescent labels used to stain other compounds were as follows: CF®488 tagged wheat germ agglutinin (WGA) from Biotium (Fremont, California) (for Chtn NF); carbohydrate binding module 3A (CBM3) from NZYtech (Lisbon, Portugal) (for ShCel NF only and not citrus fibre, as evident in Figure S1 in Supplementary material); CF®488 tagged goat anti-mouse immunoglobulin (Ig) from Biotium (for CBM3) (Peaucelle et al., 2020); and sodium 8-anilino-1-naphthalenesulfonate (ANS-Na) from Tokyo Chemical Industry Co., Ltd. (Tokyo Japan) (for CG). Distilled water or reverse osmosis water was used to prepare all samples.

2.2 Sample preparation

To study CG-NF synergy, 5% (w/w) aqueous binary mixtures of CG-NF were prepared in varied mass ratios (CG only, 9:1, 8:2, 7:3, 6:4, and 5:5) by mixing water, CG powder, original slurries of Chtn and ShCel NF, and/ or filter-dewatered CG-NF pastes (adjusted in percentage of constituents) using an IKA Eurostar stirrer (Staufen, Germany). 1.5% (w/w) diluted NF slurries were also prepared. Also, three methods of creating strong fibre-based composites with 50% (w/w) sunflower oil—with and without NF and laccase-oxidised ferulic acid (FA*)—were evaluated and as sketched in Figure 1. The total CG +/- NF content and the FA* concentration in the bulk structure were kept at 5.73% (w/w) and 1 mM, respectively. Method (Mtd) 1 was as according to sequence D in our previous paper (Tan et al., 2025): in the process of emulsifying oil into shear-activated citrus fibre slurry (using an IKA T25 Ultra-Turrax® disperser), curdlan powder was added toward the end. NF was not used in Mtd 1 due to flocculation observed in preliminary trials. To circumvent flocculation, Mtd 2 and Mtd 3 involved manual mixing of sub-composites—namely, (i) a preliminary emulsion gel template (EGt) structured by CG and citrus fibre of higher (67%) oil load, with or without FA*; and (ii) a binary phase of CG-NF in pliant paste form, with 14% (w/w) total solids. In Mtd 2, the CG-NF paste was never frozen, whereas in Mtd 3 it was reconstituted from a freeze-dried state. In further variations, the CG-NF paste was manually extruded into the EGt to form a mesh of 1 mm strands with inter-strand contact points, instead of being blended in by mixing. To prepare cooked pork subcutaneous fat reference, raw pork lard with skin was cut in thick chunks, vacuum-sealed in heat-resistant bags, and sous-vide cooked in 90◦C water for 4 h and 6 h. Cooking this way corresponded to dry air roasting of thick slabs of pork belly, which according to culinary literature would take 2 to 6 h for the interior to reach 90◦C. For

subsequent analyses, the portion without the skin was used. All samples were stored at 5◦C until analysis. Regarding the preparation of samples for compression testing, the details are stated in Section 2.6.

2.3 Small to large amplitude oscillatory shear rheology

The samples analysed were the formulated CG-NF mixtures and 50% (w/w) oil-rich composites from Section 2.2, and cooked pork fat cut that was into 1 mm thick slices by a Westmark cheese slicer (Lennestadt, Germany). Duplicates were run on an Anton Paar MCR 302 rheometer controlled by a RheoCompass™ software (v. 1.34) (Graz, Germany) within one day of sample preparation. A serrated 20-mm parallel plate geometry was used at 1 mm sample gap for good sample grip. Apart from the cooked pork fat, each sample was rapidly heat-set in situ at 25 °C/min from 20◦C to 95◦C to arrest molecular movement early and minimise phase segregation, and then cooled to 20◦C at 10 °C/min. Next, LAOS waveform data was collected across 26 strains from 0.0101% to 1010% (without causing sample rupture), at 1 rad/s and 20◦C, with 512 raw data points per full oscillatory cycle per strain. Using a MATLAB-based software called “MITlaos” (v. 2.1) (Winter & Ewoldt, 2017), the stress response in each cycle of interest was converted into Fourier components. Odd integer harmonics (n = 1, 3, …) of the Fourier spectrum were used to reconstruct a noise-filtered stress signal, which was then decomposed into elastic and viscous stresses using orthogonal Chebyshev polynomials of the first kind. From the elastic and viscous Chebyshev coefficients, e_n and v_n, equations 1 and 2 would derive at the elastic strain stiffening ratio S and the viscous shear thinning ratio (i.e., the negative of the shear thickening ratio T) to the leading order (Ewoldt et al., 2011). For more theoretical background on LAOS, other references are recommended (Cho et al., 2005; Ewoldt et al., 2008; Hyun et al., 2011; Novak, n.d.).

147 $$S = \frac{4e_3 + \cdots}{e_1 + e_3 + \cdots} \quad (1)$$

148 $$-T = -\frac{4v_3 + \cdots}{v_1 + v_3 + \cdots} \quad (2)$$

149 In addition, raw sub-composites used in Mtd 2 and Mtd 3 were tested for complex
150 viscosity within a day of preparation to determine their relative mixability. Duplicates
151 were run in amplitude sweep from 0.1% to 100% strain at 1 Hz and 20◦C, using a
152 smooth 20-mm parallel plate geometry set at 1 mm sample gap.

153 **2.4 Field electron scanning electron microscopy (FESEM)**

154 10% (w/w) aqueous suspensions of CG, CG-Chtn (in 5:5 mass ratio), and CG-ShCel
155 (in 7:3 mass ratio) were heated in a 70◦C water bath for 10 min and freeze-dried in a
156 Telstar LyoQuest -85 Plus unit (Terrassa, Spain). The freeze-dried samples were
157 examined for their morphology by SU8220 FESEM from Hitachi (Tokyo, Japan). For
158 enhanced brightness, they were priorly coated with 5 nm of platinum by a JFC-1600
159 ion splutter from JEOL (Tokyo, Japan). For CG alone, the emission current was 10.1
160 μA, the accelerating voltage was 2.5 kV, and the deceleration voltage was 1.5 kV. For
161 CG-NF, the settings were respectively reduced to 0.9 μA, 2.3 kV, and 1.3 kV. Life
162 images at magnification 50,000× were taken.

163 **2.5 Differential scanning calorimetry (DSC)**

164 For glass transition temperature (Tg) analysis, freeze-dried samples with CG-NF mass
165 ratio of 9:1, on top of samples from Section 2.4, were run in duplicates in a Netzsch
166 DSC 214 Nevio unit (Selb, Germany). In each run, 3.2-4.2 mg of sample was loaded
167 into an aluminum crucible pan with a non-pierced lid, and heated at 5 °C/min from

180◦C to 300◦C. The onset of Tg was determined using a Proteus Analysis software (v. 8) (Netzsch).

2.6 Compression stress-strain profiling

Deskinned cooked pork belly fat was cut into 2.0 × 2.0 × 1.3 cm (width, length, height). Composites with 1 mm strands were formulated by extruding the CG-NF paste of interest, through a syringe with a 1 mm tip, into a pre-weighed EGt within 2.0 × 2.0 × 1.3 cm (width, length, height) wells of a silicone mould tray. , The paste-EGt mass ratio was 1:3. Composites without strands were prepared by manually blending the EGt and the CG-NF paste at the same mass ratio in a 5 °C cold room on ice bath, followed by deposition into the same silicone tray. To heat-set the composites, the silicon tray was covered with aluminum foil and incubated in 95 °C water bath for 10 min. After which, the silicon tray was cooled in air at RT for at least 8 min before the demoulding of samples.

The heat-treated sample blocks were compressed in triplicates to 80% strain by a P/35 cylindrical flat end probe, on a Stable Micro Systems TA.XT. plus Texture Analyser (Surrey, U.K.) at RT. The test speed was 1 mm/s and the trigger force was 0.5 g. Using self-written macro functions in an Exponent Connect software (version 8.1.2.0), the change (∆) in stiffness, which indicated elasticity (Phoon et al., 2024), was calculated from the stress-strain gradient under mid strain (40-50%) and high strain (70-80%) following equation 3 (a and b = 50% and 40% strain, or 80% and 70% strain). The sample hardness was taken as the force at 80% strain.

$$\Delta Stiffness\ (kPa) = 100 \times \frac{Stress_a(kPa) - Stress_b\ (kPa)}{Strain_a(\%) - Strain_b\ (\%)} \quad (3)$$

2.7 Fluorescence imaging

To view the size of oil droplets in non-heat-set emulsion gel templates with 50% and 67% (w/w) oil load, each 25 mg sample was stained by 5 µL of 0.01% (w/v) Nile Red in ethanol on a microscopy slide and imaged under an Olympus BX53 epifluorescence microscope (Tokyo, Japan). To view the distribution of compounds in selected heat-set, multi-stained samples, each sample was sliced by a Leica CM3050 S cryotome (Leica Biosystems, Wetzlar, Germany), subjected to a series of staining and water rinsing on a microscopy slide, and imaged by confocal scanning laser microscopy on an Olympus FV3000RS. Each staining in the Nile Red solution, 0.02% (w/v) FITC in ethanol, and 1% (w/w) ANS-Na in water took 3 min. Each incubation in 0.001% (w/v) CF®488-tagged WGA in water, 0.006% (w/v) CBM3 in water, and 0.002% (w/v) CF®488-tagged goat anti-mouse Ig in water was allocated at least 20 min. All images at magnification 20× were adjusted in brightness and contrast using a Fiji software.

2.8 Statistical analysis

For the analysed parameters in Section 2.6, one-way analysis of variance (ANOVA) with post-hoc Tukey test was performed at n =3, using an online calculator (Kingdom).

3. Results and discussion

In this section, each accompanying figure facilitates comparative analysis among the various samples from a unique angle of nonlinear viscoelasticity. For instance, I_3/I_1 quantifies physical crosslinks or chain entanglements in a sample, serving as a measure for CG-NF interaction in the context of this study. Hence, a higher I_3/I_1 which corresponds to an increase in G'_1/ elastic stress/ total stress would confirm synergy, dispelling the possibility that the increase is only due to an inflated effective concentration of CG caused by the hygroscopic NF. For another example, in Lissajous

figures (i.e., elliptical plots of stress over sinusoidal strain [γ] or shear rate [$\dot{\gamma}$] on a Cartesian plane) the tilting direction in the quadrants is dependent on the phase shift of the higher harmonic. Drawing from the parallelism between Lissajous figures and distorted stress waveforms (Novak, n.d.), the tilting direction is indicative of the ease with which polymers align to shear. A further case is the elastic strain stiffening ratio S and the viscous shear thinning ratio -T. Both ratios could be mathematically defined by alternative viscoelastic moduli such as the minimum-strain modulus G'$_M$, (γ = 0), large-strain modulus G'$_L$ (γ = peak strain γ_0), minimum-rate dynamic viscosity η'$_M$ ($\dot{\gamma}$ = 0), and large-rate dynamic viscosity η'$_L$ ($\dot{\gamma}$ = peak shear rate $\dot{\gamma}_0$), as according to equations 4 and 5 (Ewoldt et al., 2011):

$$S = \frac{G'_L - G'_M}{G'_L} \tag{4}$$

$$-T = -\frac{\eta'_L - \eta'_M}{\eta'_L} \tag{5}$$

As S and -T are relative to G'$_L$ and η'$_L$, large magnitudes of S and -T need not mean high elasticity or low viscosity. On the other hand, a sample could manifest elastic and viscous nonlinearities simultaneously, adding complexity to the rheological behaviour for interpretation. The following is a discussion of different angles from intertwining perspectives. By the end of which, we attempt to draw insightful implications about the addition of Chtn and ShCel NF to fibre-structured oil, for enhanced functional prototyping of elastic animal fat mimetics.

3.1 Effect of chitin nanofibers on the elastic character of curdlan fibre network

In Figure 2a, values of shear *G'*$_1$ under small amplitude oscillatory shear (γ_0 = 0.2%, 1.0%), as generated by the RheoCompass™ software, were compared across the

binary CG-NF mixtures and their single component controls as a first check for physical synergy. In the calculation of G'_1 the software applied the assumption that, the stress response was characterisable by a sinusoidal function of the applied oscillatory frequency. Figure 2a shows that Chtn NF (as well as ShCel NF) had very low G'_1 at -1 order of magnitude (at 1.5% w/w). Despite this, Figure 2a suggests the synergising effect of Chtn, with G' increasing from below 5 kPa to above 20 kPa as the CG-Chtn mass ratio decreased to 5:5. Also, the Tg values of CG-Chtn mixtures were ≥244.8◦C and significantly higher than 242.3◦C for CG alone (Figure 2c), implying positive impact of Chtn on the stiffness of CG. The signal of CG-Chtn synergy is further corroborated by Figure 3, which shows higher I_3/I_1 values in shear stress for all the tested CG-Chtn mass ratios. Particularly, I_3/I_1 for CG-Chtn at 6:4 and 5:5 was higher than for the other samples at γ_0 below 100%.

Figure 4 depicts Lissajous figures and shear elastic stress as a function of sinusoidal strain, with higher harmonic contributions factored in. As such, compared to G'_1 it provides a more robust description of nonlinear viscoelasticity at high shear. In Figure 4c which represents the CG control, the total stress at a high γ_0 of 101% was drastically lower than at lower strains. This reflects the proneness of heat-set CG gel to fatigue (Hou et al., 2024), which could be explained by how its bundled configuration is less liable to the realignment of helices to dissipate energy, when under high shear deformation. However, in the presence of Chtn, this was not observed (Figures 4d-h), likely due to the crosslinks formed with the spatially intervening Chtn.

Figure 5 informs LAOS behaviour relating to strain stiffening/ softening and shear thickening/ thinning, through plots of normalised G'_1 and G"$_1$ and the ratios S and -T over γ_0. For CG-Chtn at 9:1 and 8:2, the weak strain overshoot in the corresponding plots of normalised G'_1 and G"$_1$ versus γ_0, (Figures 5b-c) suggests that, the minority

Chtn existed in unstable clusters under shear (Parthasarathy & Klingenberg, 1999; Sim et al., 2003). Nonetheless, as the CG-Chtn mass ratio decreased further, this disparateness in microstructure became unapparent (Figures 5d-f). Although Chtn added at any tested proportion to CG would not impact strain stiffening drastically (Figure 5g), its contribution to elastic character at high shear strain (e.g., γ_0 = 101%) was unequivocal, as evident in Figure 4a. For subsequent formulation of 50% (w/w) oil-rich composites, the 5:5 mass ratio was chosen to create a CG-Chtn paste.

3.2 Effect of cellulose nanofibers on the elastic character of curdlan fibre network

In the SEM images of Figure 2c, the fibrillar structures were reckoned to be NF, with an average fibre diameter within 10-50 nm according to the manufacturer's product specifications. On the other hand, the anticipated diameter of curdlan microfibrils following heat treatment at 70◦C was within 8.9-11.5 nm (Hou et al., 2024), and they were too fine for sharp viewing at magnification 50,000×. Unlike Chtn NF which looked tubular with higher topography contrast, ShCel NF appeared belt-like, suggesting that its configurational impact would be different. Indeed, as shown in Figure 3, the I_3/I_1 values in stress were mostly higher for CG-ShCel than for CG-Chtn mixtures (except for CG-ShCel at 9:1) at γ_0 ≤ 15.9%, suggesting more crosslinking between CG and ShCel. As would be discussed in the following, ShCel also synergised with CG, but seemingly not as straightforward as Chtn. In fact, compared to other mass ratios, CG-ShCel at 7:3 showed unusual properties.

Figure 2a shows that when the CG-ShCel mass ratio dropped from CG only to 7:3, G'_1 for γ_0 at 0.2% and 1.0% rose from below 5 kPa to 13.5 kPa and 11.2 kPa, respectively. Correspondingly, Tg increased significantly from 242.3◦C to 245.8◦C (Figure 2c).

285 However, CG-ShCel at 7:3 also had the lowest crossover strain in viscoelastic moduli
286 (i.e., 45%) (Figure 2a). At γ_0 ≥ 63.4%, its normalised total stress response was
287 drastically lower in elastic contribution than at lower strains, as denoted by the
288 Lissajous figures in Figure 4k. In the second quadrant (-, +) and fourth quadrant (+, -)
289 of the elastic Lissajous curve in Figure 4k, the pronounced curvature was indicative of
290 quasi linear viscosity and structural elements of linear topology. For which, their stress
291 waveform would have a “forward tilted stress” shape (Hyun et al., 2003) arising from
292 a phase shift δ_3 in the third harmonic stress close to 180◦ (or 270◦ phase shift φ_3
293 between the third harmonic and the fundamental stress) (Novak, n.d.). Such structures
294 were postulated to be excess ShCel NF polymers not deeply entwined into the CG-
295 ShCel network. Collectively, all this data points to CG-ShCel at 7:3 having enhanced
296 elasticity at lower strains and acting more viscous at higher strains. Yet, interestingly,
297 for γ_0 ≥ 63.4% CG-ShCel at 7:3 had consistently high I_3/I_1 values in shear stress within
298 0.27-0.31 compared to all other mass ratios of CG-ShCel (Figure 3b). This probably
299 enabled strong strain stiffening at high strains (*which could manifest effective viscous*
300 *damping*), as evidenced by the exceptionally high values of S ratio (i.e., 1.8 to 3.5, for
301 γ_0 within 63.4-253%) shown in Figure 5h. As an aside, such strain stiffening mechano-
302 response is typical in biogels but uncommon in synthetic hydrogels (Jaspers et al.,
303 2014), making CG-ShCel at 7:3 unique.

304 Then, as the CG-ShCel mass ratio decreased to 6:4, G'_1 for γ_0 at 0.2% and 1.0% fell
305 to 7.5 and 4.2 kPa, respectively. When the CG-ShCel mass ratio fell further to 5:5, G'_1
306 for γ_0 at 0.2% and 1.0% increased to 12.0 to 6.2 kPa, respectively, but never back to
307 the values associated with CG-ShCel at 7:3 (Figure 2a). For both mass ratios
308 compared to 7:3, the wider gaps in G'_1 between γ_0 at 0.2% and γ_0 at 1.0% denotes
309 the onset of nonlinear viscoelastic character at lower shear strain. However, at γ_0

310 ≥40%, the elastic contribution to their stress response was the highest (Figure 4b). In
311 Figures 5e-f, there was even faint resemblance of strong strain overshoot (i.e. Type IV
312 LAOS archetype) with a local minimum in G'_1 followed by its peak as the strain
313 increased. This indicates associative interactions probably among hydrophobic sites
314 (Hyun et al., 2011), e.g., in substantial cellulose aggregates, which did not manifest as
315 strong strain stiffening behaviour (Figure 5h).

316 Contrary to CG-Chtn at 5:5, which represented a structure with highly elastic character,
317 CG-ShCel at 7:3 represented a more viscous but strain stiffening structure when under
318 high shear. Subsequently, the 7:3 mass ratio was chosen to create a CG-ShCel paste,
319 for formulation of 50% (w/w) oil-rich composites. The impact of both CG-Chtn and CG-
320 ShCel pastes on the mechanical strength of derivative oil-rich composites was
321 dissimilar but insightful, as would be discussed in Section 3.3.

322 **3.3 Interpretation on the mechanical strength of oil-rich composites structured**
323 **by curdlan and chitin/ cellulose nanofibres, compared to cooked pork fat**
324 Oil-rich composites based on either the CG-Chtn 5:5 paste or the CG:ShCel 7:3 paste
325 from Mtd 2 attained high G'_1 at ≥ 20 kPa, for γ_0 at 0.2% and 1.0% (Figure 2b). This
326 was regardless of whether the EGt sub-composite had FA* dosed. This achievement
327 was meaningful, considering that the G'_1 for γ_0 at 1.0% was comparable to that of pork
328 fat cooked for 4 h (at 16-18 kPa, not shown), and even surpassed that of pork fat
329 cooked for 6 h (at 5-13 kPa, not shown). In contrast, Mtd 3 which used CG-NF pastes
330 reconstituted from freeze-dried mixture yielded lower G'_1 within 7.0-13.4 kPa for γ_0 at
331 0.2% and 1.0% (Figure 1b). This might be an outcome of freeze-induced fibre
332 aggregation and diminished CG-NF interaction. This postulation was supported by
333 Figure S2 in Supplementary material, which shows lower complex viscosities of CG-

NF pastes from Mtd 3 than from Mtd 2. Without NF, the complex viscosity of pure CG paste was even lower, and for its derivative oil-rich composites the G'_1 was under 7.0 kPa for γ_0 at 0.2% and 1.0% (Figure 2b). Figure 6 depicts the Lissajous figures and plots of shear elastic stress versus sinusoidal strain for the oil-rich composites and cooked pork fat. Corresponding to the thinner consistency of the pure CG paste and reconstituted CG-ShCel paste, their Lissajous figures clearly reveal higher viscous and less elastic contribution in total stress response for γ_0 at 101% and 159% (Figures 6a, b, f, i, j, n). During post-thermal LAOS deformation of their derivative composites, they likely posed less local restriction to (oil) floc size rearrangement. This reduced constraint might explain the weak strain overshoot behaviour appearing at $\gamma_0 \geq 10\%$ (Figures 5i, j, n). In contrast, the CG-Chtn 5:5 paste in Mtd 2, having no freezing history, endowed the highest extent in shear elastic character among the tested composites (Figure 6o). In its associated elastic Lissajous curves (Figures 6c, k), the curvatures in the second and fourth quadrants for γ_0 at 101% and 159% were the least pronounced, compared to the rest of the composites depicted in Figure 6.

The pork fat references cooked for 4 h and 6 h contained softened collagen and 82-85% (w/w) total fat according to additional analysis by acid hydrolysis. According to Figure 6, they were more brittle and less shear-resistant than the oil-rich composites: their Lissajous figures in Figure 6g reflect distinctly higher responsiveness to low shear strains ($\gamma_0 \leq 25.2\%$). Figure 7 compares the compressive strength among the references and the derivative oil-rich composites. From this angle, however, the pork fat cooked for 4 h displayed the highest strength, even though it underwent brittle-elastic transition with increasing compressive strain. There are two possible mechanisms for the high compressive strength in the pork fat cooked for 4 h. First, pure pork fat at RT is below its apparent melting point and typically associated with

359 densely packed beta prime (β') and beta (β) fat crystals (Zhang et al., 2023). Coupled
360 with entrapment of the fat domains within a collagen network (Figure 7a), its dense
361 microstructure could withstand compressive force (Meng et al., 2023). Second, such
362 dense microstructure could give rise to higher internal friction, as evident in the lesser
363 shear thinning behaviour of the pork fat cooked for 4 h than in oil-rich derivatives
364 (Figure 5s-t). Thus, during compressive deformation at RT, the pork fat cooked for 4 h
365 could pose more friction at the sample-probe and sample-platform contact surfaces,
366 thereby impeding crack propagation from both surfaces (ASTM C39). When
367 overcooked (i.e., to 6 h), more collagen fibres in the microstructure could have been
368 heat-dissociated to facilitate the coalescence of melted fat, leading to enlarged fat
369 domains as noticeable in Figure 7a and as had been similarly reported in literature
370 (Lian et al., 2023). The gentler stress-compressive strain gradient at 40-50% strain
371 observed for the pork fat cooked for 6 h (Figure 7a) was deduced to be because of
372 less collagen fibres for stress load distribution. Regarding the high shear failure in the
373 cooked pork fat references, we postulate that with the anticipated rigidity of highly
374 ordered molecular arrangement in fat crystals, brittleness was inevitable to dissipate
375 shear stress.

376 Contrary to the pork fat reference cooked for 4 h, the studied composites generally
377 showed weaker compressive strength although they had higher shear resistance. To
378 elaborate, their stress-compressive strain gradients at 40-50% mid strain were less
379 steep (Figures 7a, c), and their average hardness values at 80% compressive strain
380 could not reach 1879 g as observed in the pork fat cooked for 4 h (Figure 7c). This
381 might have stemmed from inadequate inter-phase bonding between the CG-NF and
382 EGt sub-composites during the heat-induced gelation of curdlan. Consequently, the
383 lesser cohesion in the bulk structure led to uneven stress distribution during

compression. In other words, the problem was reckoned an issue of the spatial distribution of components in the microstructure, rather than inadequate physical reinforcement of NF to CG. Even though the dispersed oil droplets were smaller in size than the fat domains in the pork fat reference cooked for 4 h (Figure 7a), this might be inadequate for tightness in the bulk microstructure. In addition, with Mtd 2 and Mtd 3, pores could have been introduced in the bringing of the sub-composites together. With unconfined lateral expansion of the material during compression, these pores might have served as local sites of frictional sliding and the onset of tensile stresses, which could trigger axial crack formation (Bazant, 2001). As a case in point, the higher viscosity of the CG-Chtn 5:5 paste (Figure S2) could have hampered its blending with EGt, such that its derivative oil-rich composite was susceptible to axial splitting when compressed (Figure 8a).

Noteworthily, among the oil-rich composites there were two which fared qualitatively better in terms of the average ∆stiffness under mid-compressive strain (i.e., 40-50% strain). One of them was the CG-based composite from Mtd 1 (Figure 7c, sample 9) with an average ∆stiffness of 37.2 kPa, and the preparation of which had all the curdlan dispersed during oil emulsification. The other was the CG-ShCel-based composite from Mtd 3 (without strands) (Figure 7c, sample 3) with an average ∆stiffness of 29.5 kPa. Even though it comprised nanofibre, axial splitting was not observed during slow manual compression (Figure 8b). In fact, the sample was visually as springy as the pork fat reference cooked for 4 h (see Supplementary material for video links). We reckon that the reconstituted CG-ShCel paste used was less viscous and more pliant than the other tested CG-NF pastes (Figure S2), and this eased its blending with EGt for more extensive inter-phase bonding. Interestingly, from the blending of a CG-ShCel paste with EGt, ShCel NF was found capable of partial migration to oil (Figure 9). Thus,

this raises two further possibilities behind the compressive strength of the CG-ShCel-based composite from Mtd 3. First, there might be a higher proportion of elastic stress response in the non-fat phase of the composite, stemming from an upward shift in the actual CG-ShCel mass ratio (Figures 4i-j). Second, there could be higher internal friction in the dispersed oil, due to increased viscosity or stabilisation by steric hindrance (Zhu et al., 2025).

3.4 Influence of other structuring strategies on the mechanical resemblance of oil-rich composites to springy cooked pork fat

Collectively, with FA*-induced crosslinks, the derivative oil-rich composites showed closer elastic strain stiffening behaviour to the pork fat reference cooked for 4 h, compared to composites without FA* (Figures 5q-r). Overall, FA*-dosed oil-rich composites had comparable average ∆stiffness under high-compressive strain (i.e., 70-80% strain) with that of the pork fat cooked for 4 h (Figure 7c, $p < 0.05$). (The exception was structured by CG-ShCel 7:3 paste from Mtd 2 and without strands.) This bears practical implication, since the physiological and normal mastication force is upwards of 70 N (Scully, 2002) and more associated with high-strain compression than with mid-strain compression.

The Influence of spatial distribution design at the microscale level was manifested again, through pairwise comparison of the average ∆stiffness within 70-80% strain between composites with and without 1 mm strands (Figure 7b; Figure 7c). All in all, the average ∆stiffness was higher when the CG-NF sub-composite was incorporated as a mesh of extruded strands instead of being blended in by mixing. This was most noticeable with the composite structured with strands of the CG-ShCel 7:3 paste from Mtd 3, which yielded an average ∆stiffness of 187 kPa (Figure 7c, sample 4), higher

than 126 kPa for its counterpart without strands (Figure 7c, sample 3). Even the average ∆stiffness of the pork fat cooked for 4 h (i.e., 132 kPa) was surpassed. A possible caveat was that the shear G'_1 might be reduced, considering the negative impact of prior freezing history as shown in Figure 2b. (We did not test this on the rheometer, since the 1 mm strands would be too thick for the typical gap width of a parallel probe.) Nonetheless, in the context of compressive resistance, the CG-ShCel 7:3 paste from Mtd 3 might fuse more effectively at its inter-strand contact points during the heat-induced gelation of curdlan. The resultant mesh framework, with its irregular topology (Meekel et al., 2024) and better interconnected struts for compressive stress distribution, is deduced to have improved the elastic stability of the composite during high compressive deformation. On the contrary, the CG-Chtn 5:5 paste without freezing history was more viscous (Figure S2) and probably more rigid to fuse, such that the increase in the average ∆stiffness through incorporating strands was only modest, from 121 kPa to 128 kPa (Figure 7c, samples 5-6).

The above examples suggest how the viscosity and pliancy of sub-composites interrelate with microstructural architecture, and how together they could be manoeuvred to control the compressive strength in the derivative oil-rich composites. For an all-rounded resemblance to the mechanical strength of springy pork fat, from both angles of shear and compressive resistance, a balancing act in formulation is needed.

4. Conclusion

This rheological study discovers synergy between curdlan (CG) and chitin (Chtn)/ cellulose (ShCel) nanofibres (NF) at low shear strains (γ_0 ≤1.0%) and in nonlinear viscoelastic regimes. The study also presents the application potential of this synergy

in fibre-based, 50% (w/w) oil-rich composites as strong animal fat mimetics. The formulation of the composites benefitted from a sub-composite binary paste comprising either CG-Chtn (at 5:5 mass ratio), which showed highly elastic character when heat-set, or CG-ShCel (at 7:3 mass ratio), which in contrast had a more viscous but strain stiffening behaviour under high shear. Successful heat-set composites yielded high shear G'_1 of ≥20 kPa (γ_0 ≤1.0%), similar in the order of magnitude for springy pork subcutaneous fat cooked for 4 h. Overall, these composites were more shear resistant, but also less compression resistant than the pork fat reference. Nonetheless, the CG-ShCel-based composite appeared promising in closing the gap, especially when the following strategies were in place: (i) decreased viscosity (or higher pliancy) in the CG-ShCel paste, to enhance inter-phase bonding; and (ii) incorporation of the CG-ShCel paste as an irregular mesh of extruded, interconnecting strands of 1 mm thickness, to improve the elastic stability of the composite. It could be beneficial to do more extensional tests on how an embedded mesh framework of extruded strands would impact the shear resistance in the bulk structure, and on how other (i.e., higher) CG-NF mass ratios in the binary paste might impact the mechanical strength of derivative oil-rich composites. In the formulation of the prototypes, the more complicated steps are the filter-dewatering of the curdlan-nanofibre composites and their (random) extrusion into strands within a composite. However, filtration of food pastes and cold extrusion are established processes in the industry, thus we are optimistic of their implementation in translational research toward larger scale production. In closing, this work offers reference value for creating strong, solid-like structured lipids rich in unsaturated fat, as healthier textural solutions in the meat analogue sphere toward more sustainable eating.

Declaration of interest

None.

Author statement

Pui Yeu Phoon: Funding acquisition, Conceptualisation, Supervision, Methodology, Investigation, Formal analysis, Validation, Visualisation, Writing – original draft and editing. Zhan Lun Alan Tan: Methodology, Investigation, Formal analysis, Validation, Visualisation, Writing - original draft.

Funding

This work was supported by the 2021 A*STAR Career Development Fund [project number C210812056]. The funding source is not involved in the study design; collection, analysis, and interpretation of data; writing of the report; and decision to submit the article for publication.

References

ASTM International (2015). *"ASTM C39," Standard Test Method for Compressive Strength of Cylindrical Concrete Specimens 1* (no. C). https://doi.org/10.1520/C0039.

Bai, L., Liu, L., Esquivel, M., Tardy, B. L., Huan, S., Niu, X., Liu, S., Yang, G., Fan, Y., & Rojas, O. J. (2022). Nanochitin: chemistry, structure, assembly, and applications. *Chemical Reviews*, *122*(13), 11604-11674. https://doi.org/10.1021/acs.chemrev.2c00125

Bazant, Z. (2001). Size effect on structural strength. In J. Lemaitre (Ed.), *Handbook of Materials Behavior Models* (Vol. 1, pp. 50). Academic Press. https://doi.org/10.1016/B978-012443341-0/50005-3

Chen, Z., Bian, F., Cao, X., Shi, Z., & Meng, Z. (2023). Novel bigels constructed from oleogels and hydrogels with contrary thermal characteristics: Phase inversion and 3D printing applications. *Food Hydrocolloids*, *134*. https://doi.org/10.1016/j.foodhyd.2022.108063

Cho, K. S., Hyun, K., Ahn, K. H., & Lee, S. J. (2005). A geometrical interpretation of large amplitude oscillatory shear response. *Journal of Rheology*, *49*(3), 747-758. https://doi.org/10.1122/1.1895801

Choi, M., Choi, H. W., Jo, M., Hahn, J., & Choi, Y. J. (2024). High-set curdlan emulsion gel fortified by transglutaminase: A promising animal fat substitute with precisely simulated texture and thermal stability of animal fat. *Food Hydrocolloids*, *154*. https://doi.org/10.1016/j.foodhyd.2024.110063

Dreher, J., Blach, C., Terjung, N., Gibis, M., & Weiss, J. (2020). Formation and characterization of plant-based emulsified and crosslinked fat crystal networks to mimic animal fat tissue. *Journal of Food Science*, *85*(2), 421-431. https://doi.org/10.1111/1750-3841.14993

Ewoldt, R. H., Hosoi, A. E., & McKinley, G. H. (2008). New measures for characterizing nonlinear viscoelasticity in large amplitude oscillatory shear. *Journal of Rheology*, *52*(6), 1427-1458. https://doi.org/10.1122/1.2970095

Ewoldt, R. H., Winter, P., & McKinley, G. H. (2011). MITlaos user manual version 2.2 beta for MATLAB.

Hou, X., Liu, X., Zhao, G., Zhang, B., Jiang, F., & Qiao, D. (2024). Self-assembly of curdlan molecules for the formation of thermally induced gels. *Food Hydrocolloids*, *156*, 110335. https://doi.org/10.1016/j.foodhyd.2024.110335

Hyun, K., Nam, J. G., Wilhelm, M., Ahn, K. H., & Lee, S. J. (2003). Nonlinear response of complex fluids under LAOS (large amplitude oscillatory shear) flow. *Korea-Australia Rheology Journal*, *15*(2), 97-105.

Hyun, K., Wilhelm, M., Klein, C. O., Cho, K. S., Nam, J. G., Ahn, K. H., Lee, S. J., Ewoldt, R. H., & McKinley, G. H. (2011). A review of nonlinear oscillatory shear tests: Analysis and application of large amplitude oscillatory shear (LAOS). *Progress in Polymer Science*, *36*(12), 1697-1753. https://doi.org/10.1016/j.progpolymsci.2011.02.002

Jaspers, M., Dennison, M., Mabesoone, M. F., MacKintosh, F. C., Rowan, A. E., & Kouwer, P. H. (2014). Ultra-responsive soft matter from strain-stiffening hydrogels. *Nature Communications*, *5*, 5808. https://doi.org/10.1038/ncomms6808

Jia, Y., Kong, L., Zhang, B., Fu, X., & Huang, Q. (2022). Fabrication and characterization of Pickering high internal phase emulsions stabilized by debranched starch-capric acid complex nanoparticles. *International Journal of Biological Macromolecules*, *207*, 791-800. https://doi.org/10.1016/j.ijbiomac.2022.03.142

Lei, J., Li, X., Wang, S., Yuan, L., Ge, L., Li, D., & Mu, C. (2019). Facile fabrication of biocompatible gelatin-based self-healing hydrogels. *ACS Applied Polymer Materials*, *1*(6), 1350-1358. https://doi.org/10.1021/acsapm.9b00143

Li, X.-M., Meng, R., Xu, B.-C., & Zhang, B. (2021). Investigation of the fabrication, characterization, protective effect and digestive mechanism of a novel Pickering emulsion gels. *Food Hydrocolloids*, *117*. https://doi.org/10.1016/j.foodhyd.2021.106708

Lian, F., Cheng, J.-H., & Sun, D.-W. (2023). Insight into the effect of microwave treatment on fat loss, fatty acid composition and microstructure of pork subcutaneous back fat. *LWT*, *187*, 115297. https://doi.org/10.1016/j.lwt.2023.115297

Meekel, E. G., Partridge, P., Paraoan, R. A. I., Levinsky, J. J. B., Slater, B., Hobday, C. L., & Goodwin, A. L. (2024). Enhanced elastic stability of a topologically disordered crystalline metal–organic framework. *Nature Materials*, *23*(9), 1245-1251. https://doi.org/10.1038/s41563-024-01960-7

Meng, L., Zhang, C., Wei, J., Li, L., Liu, J., Wang, S., & Ding, Y. (2023). Mechanical properties and microstructure of ultra-high strength concrete with lightweight aggregate. *Case Studies in Construction Materials*, *18*, e01745. https://doi.org/10.1016/j.cscm.2022.e01745

Novak, M. (n.d.). Non-linear oscillation testing of viscoelastic fluids. LAOS: Large amplitude oscillatory shear.

Parthasarathy, M., & Klingenberg, D. J. (1999). Large amplitude oscillatory shear of ER suspensions. *Journal of Non-Newtonian Fluid Mechanics*, *81*(1), 83-104. https://doi.org/10.1016/S0377-0257(98)00096-2

Peaucelle, A., Wightman, R., & Haas, K. T. (2020). Multicolor 3D-dSTORM reveals native-state ultrastructure of polysaccharides' network during plant cell wall assembly. *iScience*, *23*(12), 101862. https://doi.org/10.1016/j.isci.2020.101862

Phoon, P. Y., Sng, A. X. Y., Yakovlev, N., Lim, S. H., Nge, C. E., Subramanian, G. S., Gorelik, S., Kanagasundaram, Y., & Kiryukhin, M. V. (2024). Modulating elasticity of heat-set soy protein-curdlan gels by small phenolic acids. *Food Hydrocolloids*, *154*, 110054. https://doi.org/10.1016/j.foodhyd.2024.110054

Ren, Y., Wei, L., Hao Yoong, J., Miao, Z., Li, H., Cao, J., & Liu, X. (2024). Effect of variation in basic emulsion structure and polysaccharide content on the physicochemical

properties and structure of composite-based emulsion gels as cube fat mimetics. *Food Chemistry*, *434*, 137450. https://doi.org/10.1016/j.foodchem.2023.137450

Scully, C. (2002). *Physiological biting force*. Oxford University Press Inc.

Sim, H. G., Ahn, K. H., & Lee, S. J. (2003). Three-dimensional dynamics simulation of electrorheological fluids under large amplitude oscillatory shear flow. *Journal of Rheology*, *47*(4), 879-895. https://doi.org/10.1122/1.1582854

Skamniotis, C. G., Elliott, M., & Charalambides, M. N. (2017). On modeling the large strain fracture behaviour of soft viscous foods. *Physics of Fluids*, *29*(12). https://doi.org/10.1063/1.4993754

Statistical Kingdom, *ANOVA Calculator*. Retrieved December 16, 2024 from https://www.statskingdom.com/180Anova1way.html

Tan, Z. L. A., & Phoon, P. Y. (2023). Developing concentrated emulsion gel hybrids structured by natural food fibres. *Food Hydrocolloids*, *145*, 109037. https://doi.org/10.1016/j.foodhyd.2023.109037

Tan, Z. L. A., Sng, A. X. Y., Nge, C. E., & Phoon, P. Y. (2025). New insights into the strengthening of fibre-based emulsion gels by phenolic compounds. *Colloids and Surfaces A: Physicochemical and Engineering Aspects*, *704*, 135476. https://doi.org/10.1016/j.colsurfa.2024.135476

Tao, H., Guo, L., Qin, Z., Yu, B., Wang, Y., Li, J., Wang, Z., Shao, X., Dou, G., & Cui, B. (2022). Textural characteristics of mixed gels improved by structural recombination and the formation of hydrogen bonds between curdlan and carrageenan. *Food Hydrocolloids*, *129*. https://doi.org/10.1016/j.foodhyd.2022.107678

Trache, D., Tarchoun, A. F., Derradji, M., Hamidon, T. S., Masruchin, N., Brosse, N., & Hussin, M. H. (2020). Nanocellulose: from fundamentals to advanced applications [Review]. *Frontiers in Chemistry*, *8*. https://doi.org/10.3389/fchem.2020.00392

Winter, P. B., & Ewoldt, R. H. (2017). *MIT Large Amplitude Oscillatory Shear (LAOS). Using FT rheology, Chebyshev decomposition, and alternative moduli to gain physical insight (Version 2.1)*.

Xu, C., Guan, S., Dong, X., & Qi, M. (2023). Super strong gelatin/cellulose nanofiber hybrid hydrogels without covalent cross-linking for strain sensor and supercapacitor. *Composites Part A: Applied Science and Manufacturing*, *164*, 107287. https://doi.org/10.1016/j.compositesa.2022.107287

Zhang, D., Fang, Z., Hu, S., & Qiu, X. (2024). High aspect ratio cellulose nanofibrils with low crystallinity for strong and tough films. *Carbohydrate Polymers*, *346*, 122630. https://doi.org/10.1016/j.carbpol.2024.122630

Zhang, H., Nishinari, K., Williams, M. A., Foster, T. J., & Norton, I. T. (2002). A molecular description of the gelation mechanism of curdlan. *International Journal of Biological Macromolecules*, *30*(1), 7-16. https://doi.org/10.1016/s0141-8130(01)00187-8

Zhang, L., Zhang, K., Yang, H., Yue, K., Liu, R., Bi, Y., & Ma, C. (2023). Characterization of lard from different adipose tissues: Physicochemical properties, thermodynamics characteristics and crystallization behaviors. *Journal of Food Composition and Analysis*, *115*, 105021. https://doi.org/10.1016/j.jfca.2022.105021

Zhao, L., Li, J., Yin, K., Ding, Y., & Sun, L. (2024). Emulsion gels prepared from Longzhua mushroom polysaccharides with self-gelling properties as beta-carotene carriers: Stability and in vitro digestibility of beta-carotene. *International Journal of Biological Macromolecules*, *276*(Pt 1), 134110. https://doi.org/10.1016/j.ijbiomac.2024.134110

Zhou, L., Fu, J., Bian, L., Chang, T., & Zhang, C. (2022). Preparation of a novel curdlan/bacterial cellulose/cinnamon essential oil blending film for food packaging application. *International Journal of Biological Macromolecules*, *212*, 211-219. https://doi.org/10.1016/j.ijbiomac.2022.05.137

Zhou, T.-Q., Wang, X.-C., Gao, L.-Y., Yan, J.-N., & Wu, H.-T. (2024). Construction and properties of curdlan gum/gellan gum binary composite gel system. *Food Hydrocolloids*, *148*. https://doi.org/10.1016/j.foodhyd.2023.109391

623 Zhu, H., Xie, X., Xu, C., Chang, X., Wu, X.-M., & Shen, Y. (2017). Effect of bacterial cellulose
624 on freeze-thaw stability of rice starch gels. *Journal of Food Engineering and*
625 *Technology*, *6*(1), 38-47.
626 Zhu, M., Wang, H., Sun, T., Lv, J., Wang, K., Huan, S., Li, Z., Liu, Y., Liu, S., McClements, D.
627 J., & Bai, L. (2025). Plant-based Pickering emulsions using cellulose nanofibers and
628 soy protein isolate: Stabilization and high environmental resistance. *Food*
629 *Hydrocolloids*, *162*, 110943. https://doi.org/10.1016/j.foodhyd.2024.110943

Declaration of Interest Statement

☒ The authors declare that they have no known competing financial interests or personal relationships that could have appeared to influence the work reported in this paper.

☐ The author is an Editorial Board Member/Editor-in-Chief/Associate Editor/Guest Editor for this journal and was not involved in the editorial review or the decision to publish this article.

☐ The authors declare the following financial interests/personal relationships which may be considered as potential competing interests:

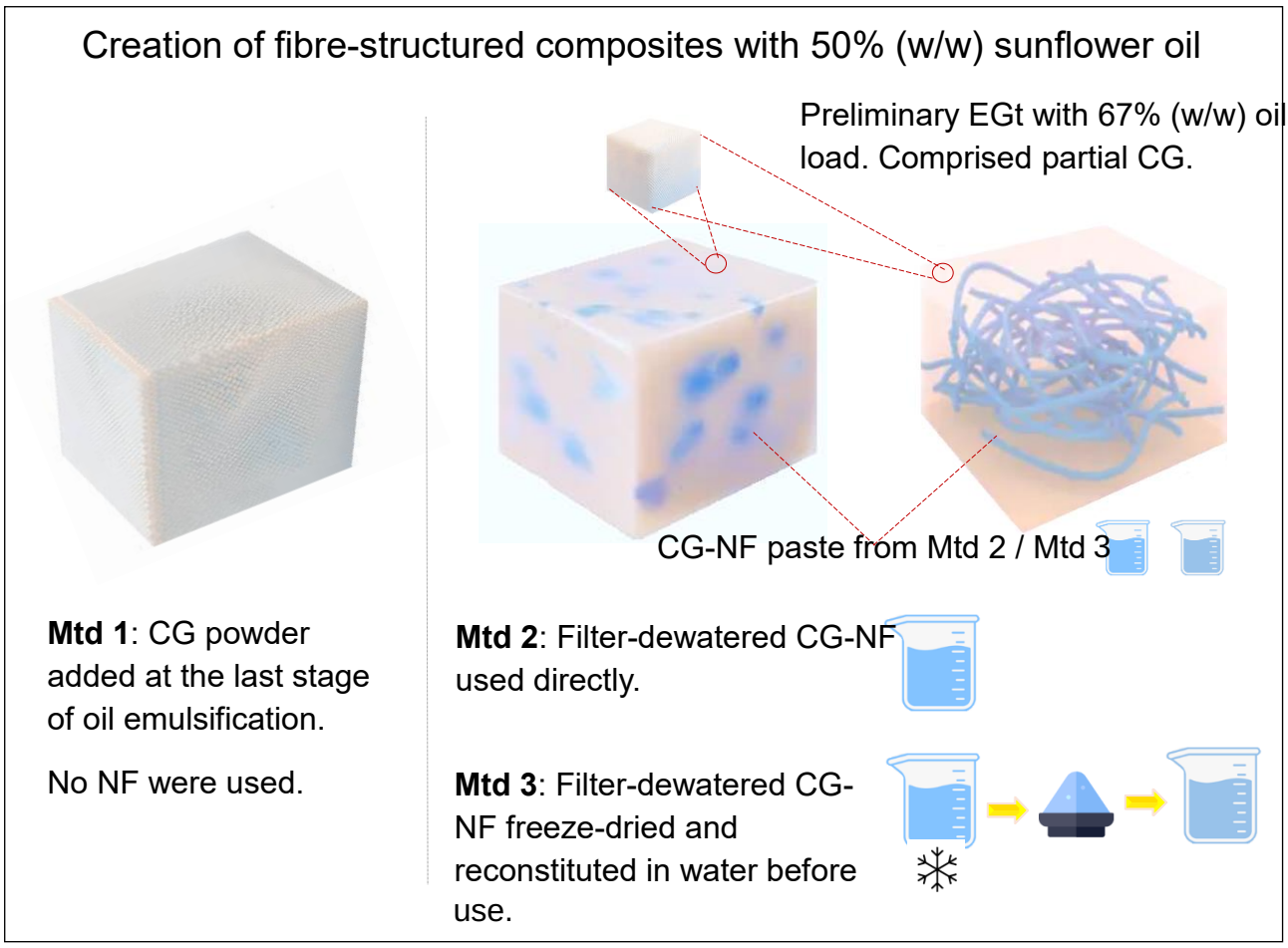

Figure 1. Sketch of the three evaluated methods Mtd 1, Mtd 2, and Mtd 3 for creating fibre-based composites with 50% (w/w) sunflower oil load. Abbreviations: CG – curdlan gum; EGt – emulsion gel template; NF – nanofibres of chitin or cellulose. The 3D graphics were generated from a licensed Rhino (version 8) software and Canva, an AI-powered online resource. The 2D icons were sourced from Flaticon.com.

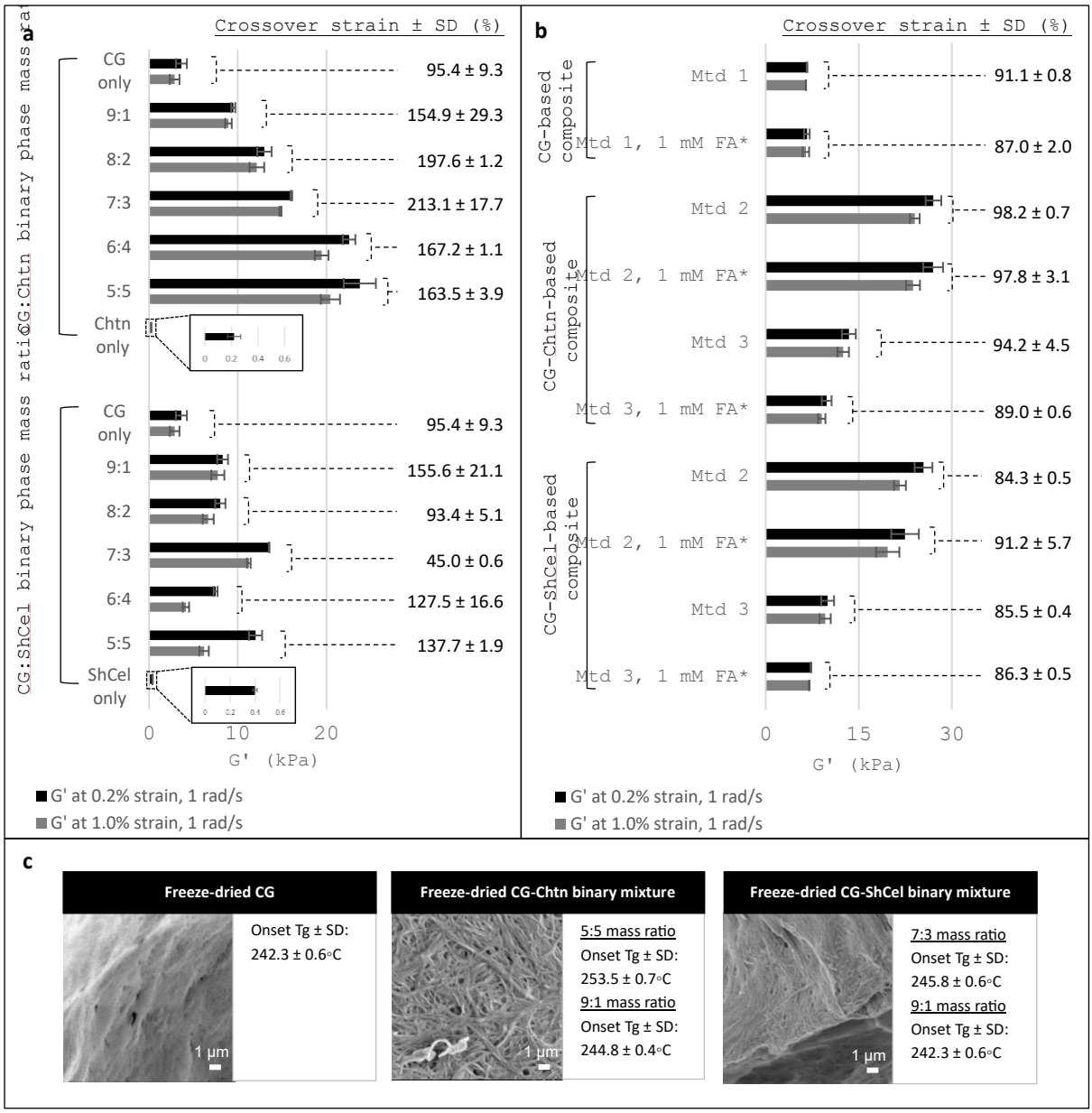

Figure 2. Influence of chitin (Chtn) and cellulose (ShCel) nanofibers (NF) on the viscoelastic moduli of curdlan (CG)-based complex systems under small amplitude oscillatory shear, and the depiction of their distribution. **(a)** Average storage modulus (G' = G'$_1$) and crossover strain (%) of 5% (w/w) aqueous binary mixtures of CG-NF at different mass ratios, compared to 5% (w/w) curdlan and 1.5% (w/w) NF controls. **(b)** Average G' and crossover strain (%) of composites with 50% (w/w) oil load formulated by different methods (mtd). **(c)** Scanning electron micrographs for heat-set and freeze-dried CG, CG-Chtn (in 5:5 mass ratio), and CG-ShCel (in 7:3 mass ratio), along with their onset glass transition temperature (Tg). Tg for CG-NF in 9:1 mass ratio was also displayed. Scale bar: 1 µm. Magnification: 50000× Other abbreviations: SD - standard deviation; FA - ferulic acid. *Laccase-oxidised.

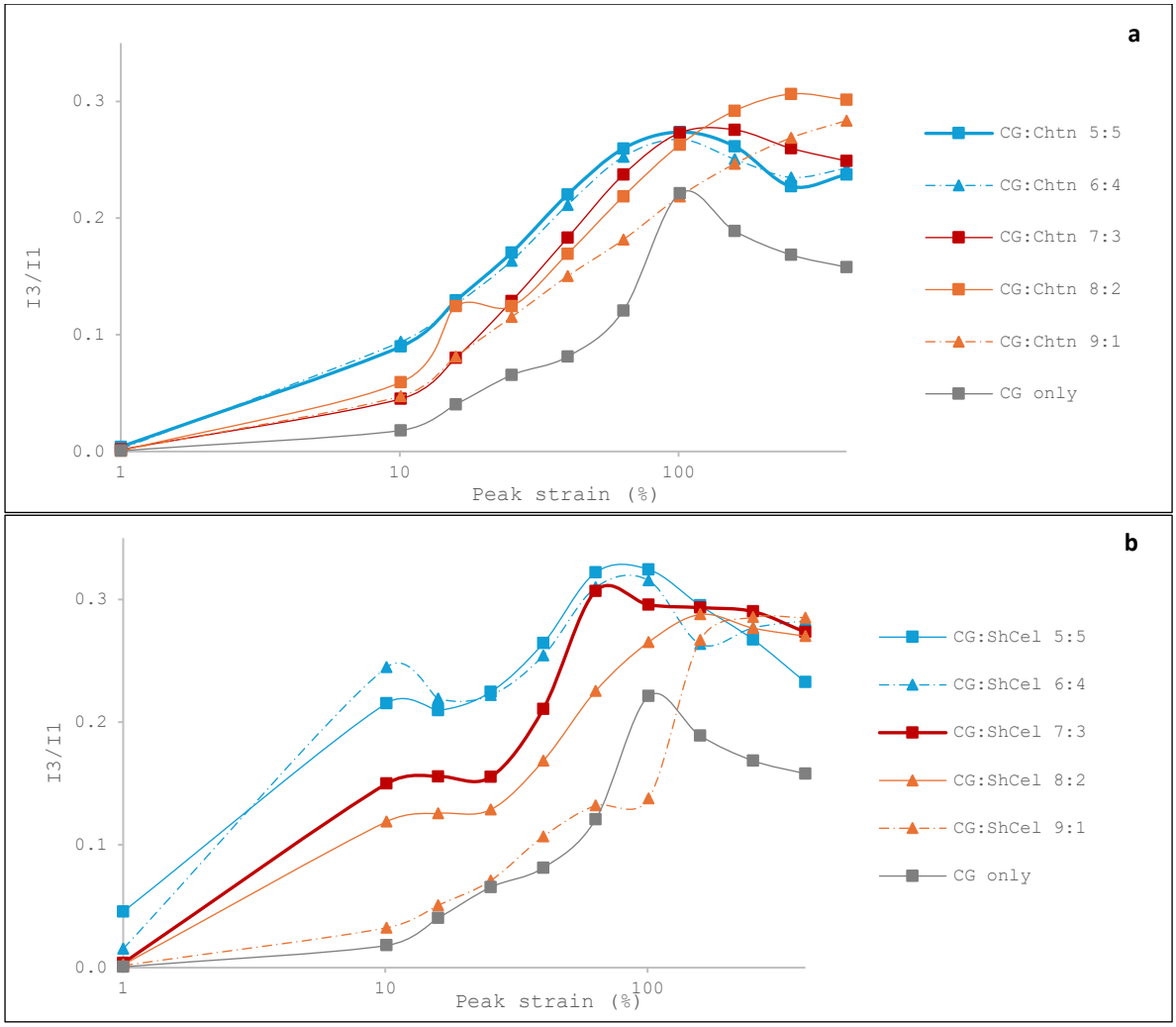

Figure 3. Representative, relative intensity of the third harmonic in shear stress I3/I1 in curdlan (CG)-based complex systems, in response to the peak strain applied during oscillatory shear. The intensity was normalised by the first harmonic in shear stress. The systems had 5% (w/w) total solids in water, comprising CG with or without **(a)** chitin (Chtn) nanofibres and **(b)** cellulose (ShCel) nanofibres at different mass ratio. The data was based on measurements at 20°C immediately after a rapid heat-cool cycle of 20-95-20°C which induced irreversible heat setting of the CG gel.

Figure 4

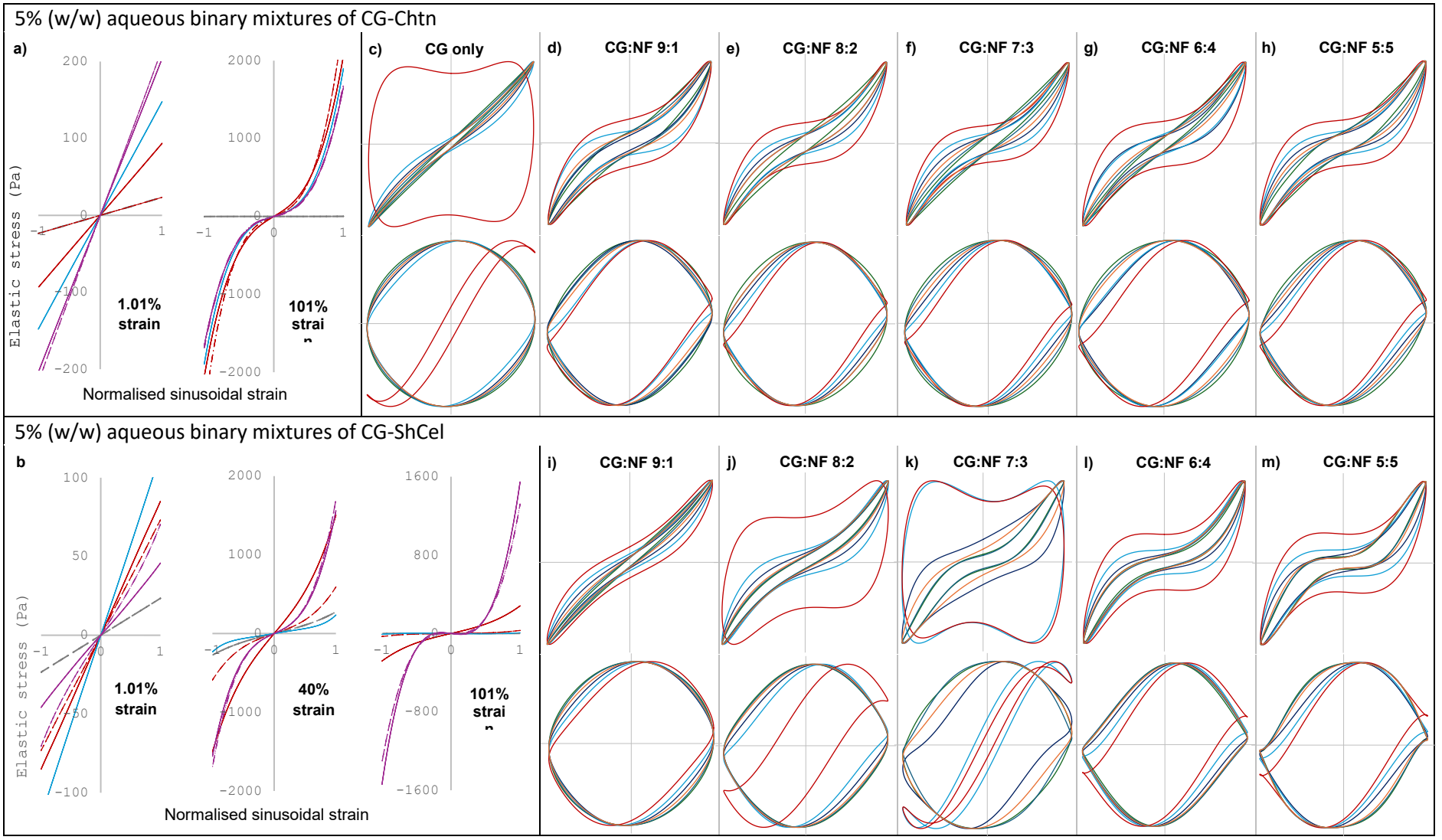

Figure 4. LAOS analysis of curdlan (CG) with and without chitin (Chtn) or cellulose (ShCel) nanofibres (NF), at different mass ratios and 5% (w/w) total solids, based on measurements at 20◦C immediately after a rapid heat-cool cycle of 20-95-20 ◦C. **(a)-(b)** Representative plots of elastic stress versus normalised sinusoidal strain at 1 rad/s, under peak strain γ_0 of 1.01%, 40%, and 101%. **(c)-(m)** Representative Lissajous figures of normalised total stress versus normalised sinusoidal strain (top row) and normalised sinusoidal strain rate (bottom row). Any normalisation of data was to the maximum intracycle stress/ strain/ strain rate. Key for CG:NF ratios in (a)-(b): — · — · CG only; ——— 9:1; — · — · 8:2; ——— 7:3; ——— 6:4; — · — · 5:5. Colour key for different strains in (c)-(m): ■ 10.1%; ■ 15.9%; ■ 25.2%; ■ 40%; ■ 63.4%; ■ 101%

Figure 5

Click here to access/download;Figure;Figure 5_old Fig S2.docx

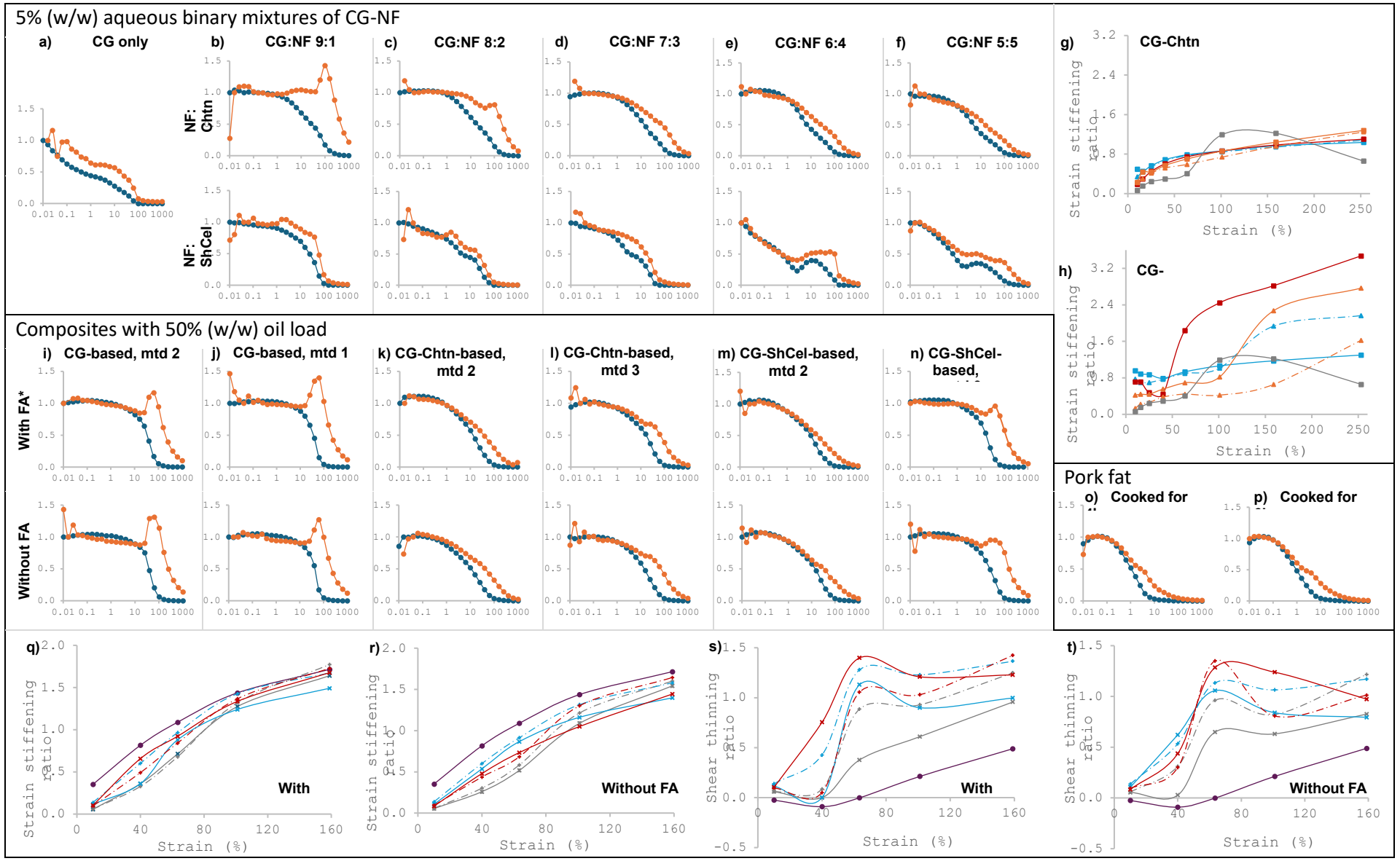

Figure 5. Strain stiffening/ softening and shear thickening/ thinning behaviour in binary mixtures of curdlan (CG) and chitin (Chtn) or cellulose (ShCel) nanofibres (NF), and derivative composites of 50% (w/w) oil load in comparison to cooked pork fat. The analysis was based on measurements at 20 ◦C immediately after a rapid heat-cool cycle of 20-95-20 ◦C. In the CG-NF binary mixtures, the mass ratio was varied within a fixed total solid content of 5% (w/w). In the oil-rich composites, NF was incorporated as part of a CG-Chtn (5:5 mass ratio) or CG-ShCel (7:3 mass ratio) paste. **(a)-(f), (i)-(p)** Representative plots of normalised first harmonic shear storage modulus (____ G'_1) and viscous modulus (____ G''_1) versus peak strain γ_0 (%). **(g)-(h)** Representative plots of strain stiffening ratio versus peak strain γ_0 (%) for CG alone and the CG-NF binary mixtures. Key: ____ CG only; _ . _ . CG-NF 9:1; ____ CG-NF 8:2; ____ CG-NF 7:3; _ . _ . CG-NF 6:4; ____ CG-NF 5:5. **(q)-(t)** Representative plots of strain stiffening and shear thinning ratios versus peak strain γ_0 (%), for the oil-rich composites compared against cooked pork fat. Key: ____ pork fat cooked 4h; ____ CG-based, Method (Mtd) 1; _ . _ . CG-based, Mtd 2; ____ CG-Chtn-based, Mtd 2; ; _ . _ . CG-Chtn-based, Mtd 3; ____ CG-ShCel-based, Mtd 2; _ . _ . CG-ShCel-based, Mtd 3. Other abbreviations: FA - ferulic acid; FA* - laccase-oxidised ferulic acid.

Figure 6

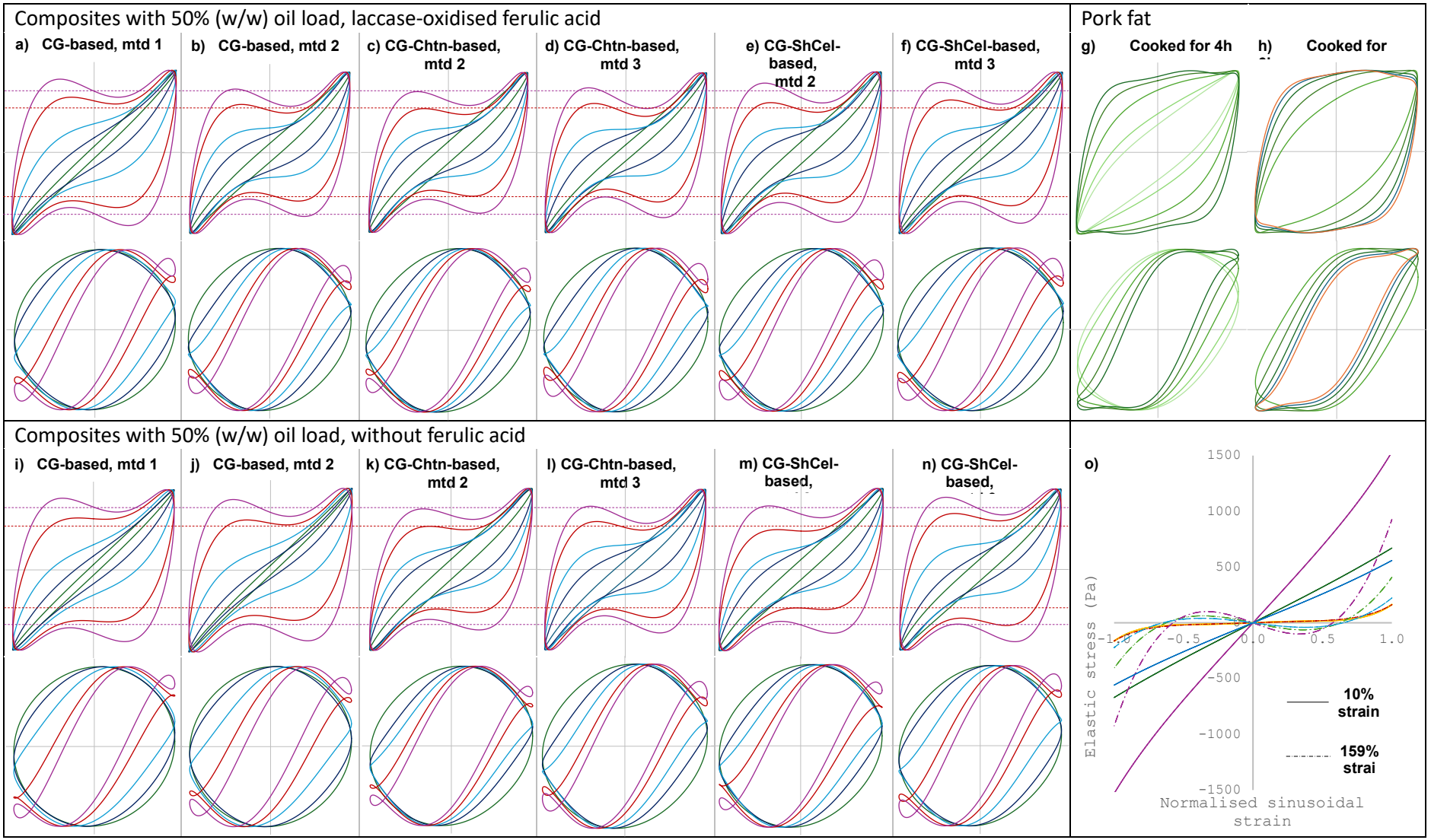

Figure 6. LAOS analysis of curdlan (CG)-based composites with 50% (w/w) oil load structured by curdlan (CG) with and without laccase-oxidised ferulic acid, based on measurements at 20◦C immediately after a rapid heat-cool cycle of 20-95-20◦C. In some of them, chitin (Chtn) or cellulose (ShCel) nanofibres (NF) were incorporated as part of the sub-composite CG-Chtn 5:5 paste or CG-ShCel 7:3 paste. Comparative analysis was done against cooked pork fat references. **(a)-(n)** Representative Lissajous figures of normalised total stress versus normalised sinusoidal strain (top row) and normalised sinusoidal strain rate (bottom row). Any normalisation of data was to the maximum intracycle stress/ strain/ strain rate. **(o)** Representative plots of elastic stress versus normalised sinusoidal strain at 1 rad/s, under peak strain γ_0 of 10% and 159%. Colour key for different strains in (a)-(n): 1.59%; 2.52%; 4%; 6.34%; 10.1%; 15.9%; 25.2%; 40%; 63.4%; 101%; 159%. Key for composites and pork fat in (o): pork fat cooked for 4h; pork fat cooked for 6h; CG-based, method (Mtd) 1 (γ_0 = 10%); CG-based, Mtd 1 (γ_0 = 159%); CG-Chtn-based, Mtd 2 (γ_0 = 10%); CG-Chtn-based, Mtd 2 (γ_0 = 159%); CG-ShCel-based, Mtd 3 (γ_0 = 10%); CG-ShCel-based, Mtd 3 (γ_0 = 159%).

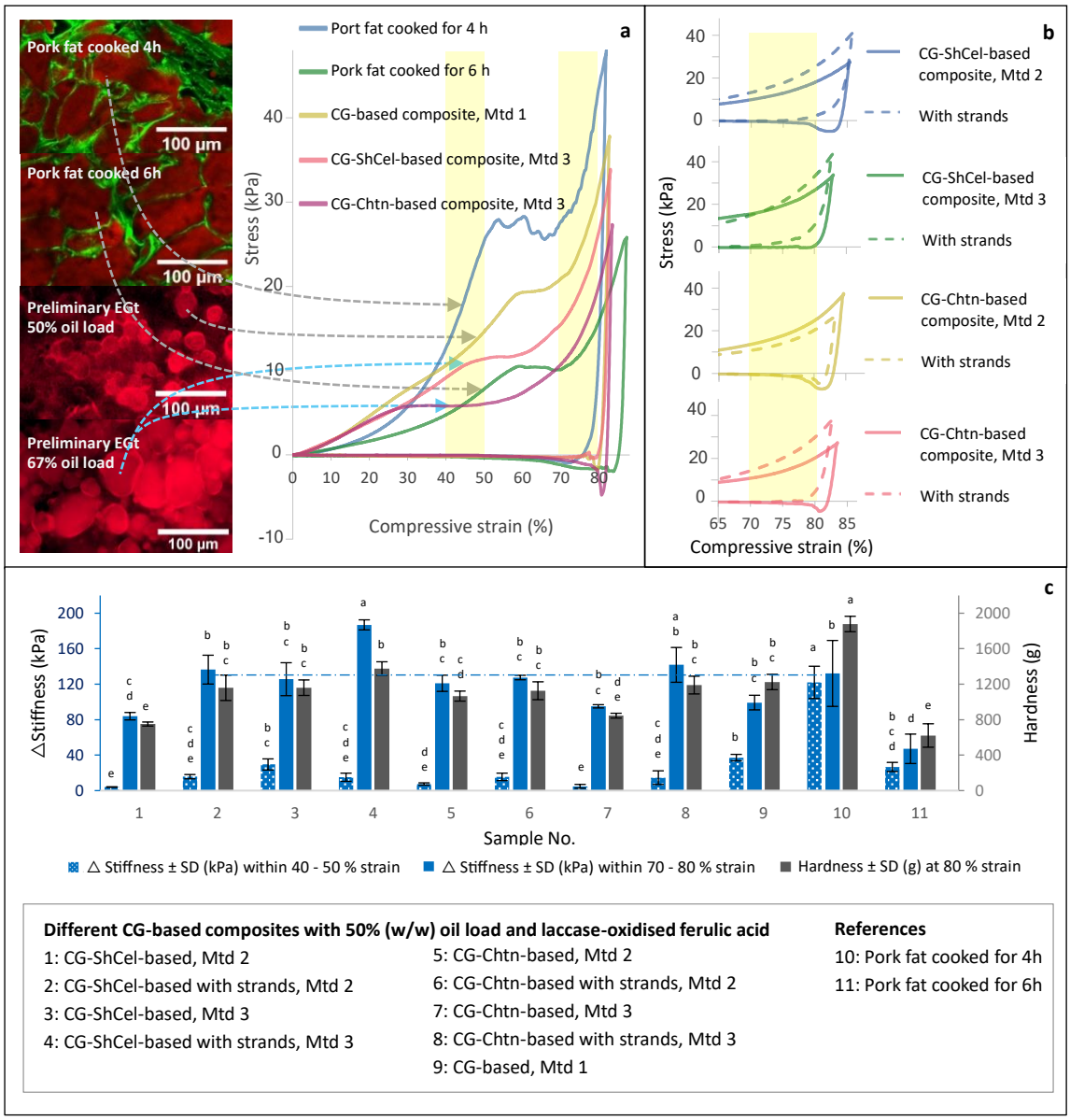

Figure 7. Representative stress-compressive strain behaviour of cooked pork fat and heat-set composites with 50% (w/w) oil load, structured by curdlan (CG) with or without chitin (Chtn)/ cellulose (ShCel) nanofibres (NF). The test speed of compression was 1 mm/s. **(a)** Stress-strain profiles of selected composites (without 1 mm strands) and epifluorescence micrographs of their constituting emulsion gel templates, compared against cooked pork fat. Scale bar: 100 µm. Magnification: 20× **(b)** Stress-strain profiles of selected composites with and without 1 mm strands, under high strain (70-80%). **(c)** Bar chart of the average change (Δ) in stiffness within 40-50% strain and 70-80% strain and the hardness at 80% strain, in cooked pork fat and various composites. The results were analysed by one-way ANOVA with Tukey post-hoc test ($p < 0.05$). SD - standard deviation.

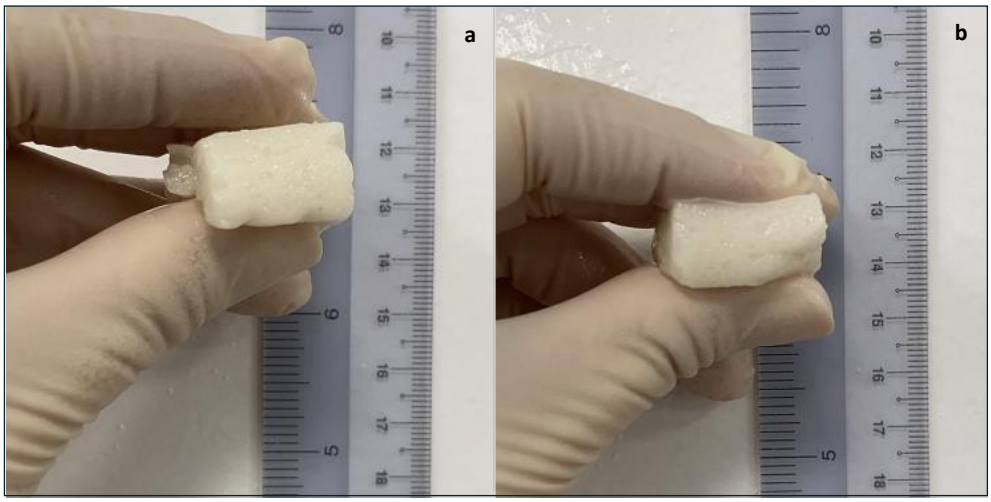

Figure 8. Slow manual compression of heat-set composites with 50% (w/w) oil load structured by curdlan (CG) with **(a)** chitin (Chtn) nanofibre (NF) or **(b)** cellulose (ShCel) NF. The sample in (a) was prepared using a CG-Chtn paste at 5:5 mass ratio without freezing history, as according to method 2 in the study. The sample in (b) was prepared using a reconstituted CG-ShCel paste at 7:3 mass ratio (there was prior freeze drying), as according to method 3 in the study. The samples did not have 1 mm strands.

Figure 9 Click here to access/download;Figure;Figure 9_fr old Fig 1.docx

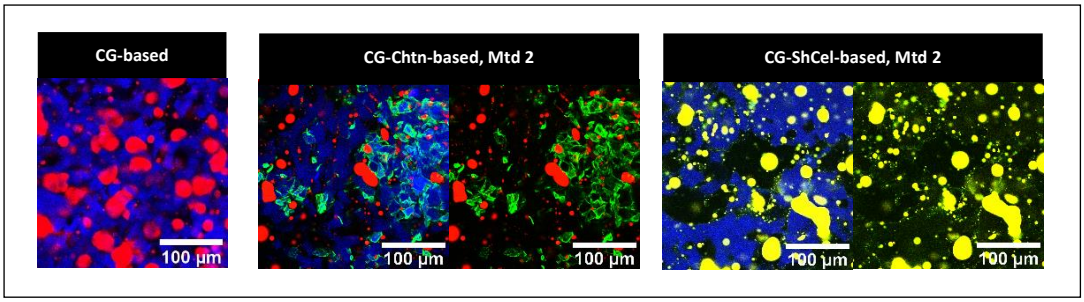

Figure 9. Merged confocal laser scanning micrographs for oil-loaded composites structured by curdlan (CG), with and without chitin (Chtn) or cellulose (ShCel) nanofibres (NF). Colour key: blue – CG stained by sodium 8-anilino-1-naphthalenesulfonate; red - sunflower oil stained by Nile Red; green – NF stained by CF®488 tagged conjugates; yellow – co-localisation of oil and NF. Scale bar: 100 µm. Magnification: 20×